Contact based void partitioning to assess filtration properties in DEM simulations

O'Sullivan, C., Bluthé, J., Sejpar, K., Shire, T., and Cheung, L. Y. G.

Abstract

Discrete element method (DEM) simulations model the behaviour of a granular material by explicitly considering the individual particles. In principle, DEM analyses then provide a means to relate particle scale mechanisms with the overall, macro-scale response. However, interpretative algorithms must be applied to gain useful scientific insight using the very large amount of data available from DEM simulations. The particle and contact coordinates as well as the contact orientations can be directly obtained from a DEM simulation and the application of measures such as the coordination number and the fabric tensor to describe these data is now well-established. However, a granular material has two phases and a full description of the material also requires consideration of the voids. Quantitative analysis of the void space can give further insight into directional fabric and is also useful in assessing the filtration characteristics of a granular material. The void topology is not directly given by the DEM simulation data; rather it must be inferred from the geometry of particle phase. The current study considers the use of the contact coordinates to partition the void space for 3D DEM simulation datasets and to define individual voids as well as the boundaries or constrictions between the voids. The measured constriction sizes are comparable to those calculated using Delaunay-triangulation based methods, and the contact-based method has the advantage of being less subjective. In an example application, the method was applied to DEM models of reservoir sandstones to establish the relationship between particle and constriction sizes as well as the relationship between the void topology and the coordination number and the evolution of these properties during shearing.

Introduction

Discrete element method (DEM) analyses generate a large amount of information about the particle-scale mechanics of granular materials. Interpreting DEM analyses at the particle scale to extract meaningful information is not always straightforward. Typical scalar particle scale metrics considered include the coordination number and the mechanical coordination number (e.g. Thornton [1]). Anisotropy can be determined by applying the second order fabric tensor proposed by Satake [2] to the contact normal orientations or the branch vector orientations. The topology of the void space emerges indirectly from the DEM simulation data; that is the void space is defined by the particle positions. In comparison with consideration of the particle and contact orientations, there has been less quantitative analysis of the void space.

This contribution firstly discusses the available algorithms to characterize and partition the void space. Then a 3D contact-based partitioning approach inspired by the 2D work of Li and Li[3] is presented. The research was originally motivated by a desire to better understand the filter properties of granular materials, and the focus is on estimating the size and orientation of the constrictions between the individual voids. The three-dimensional simulations of Barreto [4] are used in a benchmark study to compare the new approach with the algorithms proposed by Reboul et al. [5] and Dong and Blunt [6]. Cheung [7] developed two DEM models of cemented sand to study the problem of sand production in reservoir sandstones. Quantifying constriction sizes is important in this application and so Cheung's dataset is used to demonstrate the usefulness of the new algorithm.

Existing void characterization algorithms:

An early example of a void characterization algorithm is given in Oda et al. [8]. As discussed by Ghedia and O'Sullivan [9], application of this algorithm requires conversion of the DEM data set to an image file comprising pixels. In addition, the individual voids must be distinguished and Ghedia and O'Sullivan applied a watershed segmentation approach (Beucher and Lantuejoul [10]). To date the scan-line algorithm's application has been restricted to two-dimensional (2D) analyses and extrapolation to 3D would be complex. However, Li and Li [3] cited contact based approaches proposed by Tsuchikura and Satake [11] and Konishi and Naruse [12] and presented an approach to identify and partition the void space into a tessellation of void cells and this method is, in principle, more amenable to 3D application.

Real granular materials of interest in engineering practice are three-dimensional and so there is a real need for algorithms that can characterize the void space in 3D. In 3D the void space forms a continuous network and analyses must carefully consider the segmentation or separation of individual voids. Few three dimensional methods to partition the void space have been reported in the literature. Reboul et al. [5] identified individual voids from data obtained in DEM simulations by applying a

weighted Delaunay triangulation to the particle centroids, using a criterion proposed by Al Raoush et al. [13] to merge tetrahedra and identify voids. The merging criterion considers the overlap between the two spheres inscribed between the tetrahedra defining two adjacent voids. Shire et al. [14] applied this algorithm to study the anisotropy of the internal structure of granular materials subject to a general (3D) stress state and Shire [15] used the algorithm to study the general filtration properties of granular materials. In both cases the constrictions, i.e. the boundaries separating adjacent voids, were considered. While this method is very attractive, the user must decide on a threshold inscribed-sphere overlap for void merging. There is an ambiguity as to what is the correct overlap to use, and Shire [15] showed the resulting constriction size distributions (CSDs) are sensitive to the overlap specified. Shire et al. [16] showed that just as in the 2D case, the 3D DEM dataset can be converted to an image file, comprising voxels, and algorithms proposed for void analysis of micro computed tomography data (e.g. Dong and Blunt [6]) can be applied. This approach, however, is sensitive to the digitized image resolution, i.e. the ratio of voxel size to particle size [16]. In this contribution a new algorithm is proposed that overcomes some of the sensitivity issues with the Reboul et al. [5] and Dong and Blunt[6] approaches.

Contact based void partitioning algorithm

Li and Li [3] proposed a method to construct particle and void graphs for 2D DEM simulation datasets that involves a Delaunay triangulation of the contact points. The remaining triangles are selectively merged to form a space-filling tessellation of solid and void elements. In the Li and Li approach, the 2D nature of the material considered means that each void is surrounded by a closed loop of particles and so is objectively defined. Taking the method proposed by Li and Li [3], and considering 3D datasets the main additional complication is that the void space is continuous and so the partitioning must include a criterion to segment the void space into individual voids. The 3D algorithm described here was developed and implemented using MATLAB [17]. The void identification algorithm takes as input the particle centroids, radii, a list of contacting particles and the contact coordinates. The main output is information on the boundaries between individual voids, i.e. the constrictions, sometimes termed the “pore throats” in petroleum engineering applications. For the current implementation the algorithm identifies planar constrictions and outputs the constriction sizes, the constriction coordinates and the normal orientations of the constrictions. The triangulation of the contact points used the MATLAB function delaunayTriangulation which generated a tessellation of tetrahedra. If the sample boundary is included in the triangulation, a number of highly elongated tetrahedra form. To overcome this problem, just as was the case with Shire et al. [14], the outer 10% of the sample on each side was removed from consideration.

Following triangulation, the solid elements were identified to be those tetrahedra for which the four particle pairs, defining the contacts and vertices, all have one particle in common, i.e. the particle pairs defining the vertices are *A-B*, *A-C*, *A-D* and *A-E*, where A to E are letters identifying the particles. The tetrahedra meeting this criterion are entirely enclosed within a solid particle. While searching for the solid tetrahedra a set of very flat tetrahedra that define some of the constrictions are also identified. Four different particles are associated with the vertices of each of these flat tetrahedra, i.e. the union of the set of particles making up the vertices is a set of 4 unique indices, *A, B, C* and *D*. Referring to Figure 1, each of these four particles is then in contact with exactly 2 of the other particles. These "constriction tetrahedra" are almost planar and are classified as 4-point constrictions.

Both the solid tetrahedra and the constriction tetrahedra are excluded from consideration in the next step in the algorithm. The remaining tetrahedra are members of void cells and each of these void-space tetrahedra are coloured by assigning identifying integers. Using a simple permutation, the four faces associated with the 4 vertices defining each remaining tetrahedron can be found. The analysis progresses by looping over all the other tetrahedra to find the neighbouring tetrahedra that have faces that are shared with the current tetrahedron. The removal of solid and constriction tetrahedra means that there will be fewer than four neighbouring tetrahedra that are members of void cells in many cases and so not all faces are "shared" by two void forming tetrahedra. Referring to Figure 2(a), when the tetrahedron face is contained within a solid particle, and the three vertices involve three particle pairs *A-B*, *A-C* and *A-D* the tetrahedron face clearly is a void boundary (that is not a constriction) and these faces are excluded from further consideration.

Each shared face in the system is then considered in turn to determine whether the tetrahedra meeting at that face form part of a single void and should be merged. As previously noted in the Li and Li[3] 2D implementation each void cell is completely enclosed by a closed loop of contacting particles and so no explicit consideration of criteria to define a void boundary is needed. However in 3D specific rules are needed to identify the constrictions that form the boundaries to the voids. These rules are applied by considering sets of 3 or 4 contacting particles whose contacts form closed loops as illustrated in Figure 2. Referring to Figure 2(b) a "3-particle constriction" is identified when the shared face is defined by a closed loop of three contacts resulting in three particle pairs *A-B, B-C* and *C-A,* involving only three particles. The two tetrahedra meeting at this face are considered to be at either side of a void boundary and so are not merged. When the shared tetrahedron face is defined by contacts *A-B*, *B-C* and *C-D* a test is carried out to establish if *A* and *D* contact and if that is the case a closed loop of four contacts, giving a set defined as *A-B*, *B-C*, *C-D*, and *D-A* is taken to be a 4-particle constriction. Figure 2(c) illustrates a valid "4-particle constriction" denoting a boundary between two voids. Figure 2(d) indicates a scenario where *D* and *A* do not contact and so the shared face does not

define a constriction and the two tetrahedra meeting at the shared face are merged to form a single void (i.e. both tetrahedra are assigned the same colour index).

The study of void partitioning in three dimensions was motivated by a broader research agenda that aims to better understand the filtration capacity of granular materials and so, once the constrictions have been identified a measure of constriction size was sought. Here the constriction size is taken to be the diameter of the largest disk that can fit in the constriction. Considering the constrictions defined by three contact points, referring to Figure 3(a), a disk that is tangent to all three spheres was found by solving a minimization problem and the diameter of this tangent disk is taken as the constriction size. The relevant equations are given as equations 1 and 2 in Reboul et al. [5]. The resultant disk is in the plane defined by the centroids of the three spheres and it does not always lie in the plane defining the three contacts, as illustrated in Figure 3(a). Referring to Figure 3(b), for the 4-particle constrictions the constriction disk will always be tangent to spheres *B* and *C* as each of these spheres participates in two of the vertices of the tetrahedron face defining the constriction and the tetrahedron edges intersect both these spheres. Then a disk that is tangent to sphere *A* is sought, if this disk overlaps with the fourth sphere (*D*), it is considered invalid (Figure 3(b)). If the first fitting attempt yields an invalid constriction disk, the disk tangent to *B*, *C* and *D* is sought and taken to define the constriction (Figure 3(c)). In the 4-particle case the constriction disk and the tetrahedron face defining the constriction are not always co-planar. Care must be taken when the sample is very polydisperse, i.e. it contains a range of particle sizes. In this case, for the 4-particle constrictions there may be two disks tangent to spheres *A, B,* and *C* and so a constrained optimization is required, as shown in Figure 3(d). (These 4-particle constrictions include the flat constrictions illustrated in Figure 1). When all the disks are found a check is carried out to see if they are on the correct side using a dot product of every two pairs of vectors joining the centre of the void disk and the particle centroids. If all the dot products are positive, the disk position is incorrect, if two of the four dot products are positive it is correct. Then a constrained optimization is applied to this relatively small number of cases only, using a single, lower bound as the constraint. The constrained optimization affected a fraction of 1% of the constrictions for the Saltwash sample discussed below. Another point to note is that sometimes three particles can define two different 4-particle constrictions or two different tetrahedron constrictions. In these cases the duplicate constrictions are merged and those three particles are considered to represent only one constriction. In all cases the constriction disks define the constriction diameters and the constriction normal orientations are the normals to these disks.

Benchmarking against alternative methods

Shire et al. [14] applied the Reboul et al. [5] algorithm to the simulations detailed by Barreto [4] and Barreto & O'Sullivan[18] and these data were revisited here to enable comparison of the proposed method to alternative algorithms. The particle size distribution (PSD) of the spheres in these DEM

simulations matched physical glass bead samples, and is given in Figure 4, considering cumulative distributions, i.e. percentage of total volume smaller than a given size . The samples were created by generating a cloud of 4000 non-contacting spheres with random locations within a periodic cell. The samples were compressed isotropically and monotonically to a mean normal stress of 200 kPa, with a coefficient of friction of μ=0.325. This created a relatively loose sample (e=0.588). Changing the coefficient of friction to μ=0.0 and recompressing to 200 kPa yielded a slightly denser sample, with e=0.529. Note that the range of attainable void ratios is limited for these spherical particles with such a narrow particle size distribution. Stress and strain control during isotropic compression and subsequent shearing followed the approach for periodic cell simulations outlined by Thornton [19]. The constriction size distributions (CSDs) for both the loose and dense samples at the isotropic stress state were determined using the weighted Delaunay (WD) method proposed by Reboul et al. [5], the maximal ball (MB) method proposed by Dong and Blunt [6], and the new contact based method (CM) outlined here. These CSDs are cumulative distributions of the constriction size by number. The computational cost (i.e. RAM requirements) restricted consideration to a central volume of 600 x 600 x 600 voxels as input to the Dong and Blunt code, as the ratio of particle size: voxel size was 50; this meant that the number of particles considered was about 767 for the dense sample and 739 for the loose sample. The CSDs for these smaller samples are given in Figures 4(a) and (c) and Table 1. Figures 4(b) and (d) consider the application of the weighted triangulation method and the contact-based method to the entire sample of particles. Table 1 summarizes the data, and extracts the values for key points along the CSDs. C_{50} is the size for which 50% of the constrictions (by number) are smaller; C_{85} is the size for which 85% of the constrictions (by number) are smaller, etc. It is clear that the maximal ball method underestimates the constriction sizes in comparison with the two other methods. The weighted Delaunay method gives a smaller range of constriction sizes in comparison with the contact based method, whether the sub-volume or the full sample is considered. The weighted Delaunay CSD has a similar range to the contact-based method; when used with 0% overlap the CSD is at the lower end of the contact-based method range and with 100% overlap it is at the upper end of the range. All methods register a decrease in the number of constrictions when the sample density reduces, however there is no noticeable change in the CSDs. It is difficult to directly compare the numbers of constrictions determined as there were slight differences in the volumes considered for the three methods.

For the larger, full volume, dense sample the constrictions calculated using the weighted Delaunay method (50% overlap) and the contact based method were directly compared. 97% of the 3 particle constrictions identified in the contact based method were present in the weighted Delaunay dataset, while 60% of the 4 particle constrictions identified in the contact based method were present as constrictions in the weighted Delaunay dataset. In summary there was very close agreement on the

relatively objective 3-particle constrictions and less agreement on the more ambiguous 4-particle constrictions.

Data from a constant mean stress tests triaxial compression test were also considered. As described in Shire et al. [14], the contact normal orientations and the constriction normal orientations at a deviator strain of ε_d=10% were determined , where

$$\varepsilon_d = \frac{2}{\sqrt{6}} \sqrt{(\varepsilon_1 - \varepsilon_2)^2 + (\varepsilon_2 - \varepsilon_3)^2 + (\varepsilon_3 - \varepsilon_1)^2} \quad (1)$$

and ε_1, ε_2, and ε_3 are the major, intermediate and minor principal strains respectively. These orientations are plotted as rose diagrams in Figure 5. Figures 5 (a) to (c) present the contact normal orientations in the XY, XZ and YZ planes respectively, the shading of each angular bin indicates the magnitude of the average contact force orientated within that bin, normalized by the overall average contact force. The sample is compressed in the vertical (Z) direction. As would be expected in triaxial compression, the contact normal orientations are largely isotropic in the horizontal XY plane, there is a preferential orientation of contact normals in the vertical direction, and the forces transmitted in this direction are clearly larger than those transmitted via the horizontally orientated contacts. The constriction orientation distributions observed are similar for both the weighted Delaunay (WD) method and the new, contact-based method (CM). In both cases it is difficult to identify any particular pattern in the orientations when all constrictions are considered. However the constrictions with contact orientations in the direction of the major principal stress tend to be larger (i.e. above average in size). C_{15} is defined to be the constriction diameter such that 15% of the constrictions by number are smaller than C_{15}. C_{15} was selected for consideration as it allows explicit consideration of the smaller constrictions which are of interest as they significantly influence the filtration capability of the material. Referring to Figures 5(g) to (i) and Figures 5(m) to (n), if consideration is restricted to consider only those constrictions smaller than C_{15}, there are clearly a large number of these constrictions orientated in the horizontal direction, and this trend is captured in both approaches to defining the constrictions. It is clear that, in agreement with the conclusions of Shire et al. [14] the constriction normals for the larger constrictions are orientated in the direction of the major principal stress (i.e. they act in same direction as the dominant orientations for the contact normals). Shire et al. attributed this bias in the constriction orientations to the opening up of elongated voids between the discrete strong force chains orientated in the direction of the major principal stress.

Application to Cemented Sand Simulations

Cheung et al.[20] and Cheung [7] discussed DEM simulations of high-pressure triaxial compression tests on samples of Castlegate and Saltwash sandstones. The objective of this earlier study was to calibrate DEM models to study sand production. Sand production involves the migration of sandstone particles with fluid during the extraction of hydrocarbons from reservoir sandstones. Identification of the constriction size distribution is useful to assess whether the model could capture sand production due to a suffusive movement of smaller particles through the void network, or whether a plastic failure of the model rock would be required (where regions of the material would become dislodged) to produce sand. The DEM simulations were performed using the PFC3D program and the parallel bond model, described by Potyondy and Cundall [21] was used. As discussed in detail in Cheung et al. [20], the parallel bond acts alongside a contact model and so the simulation takes a number of input parameters, as listed in Table 2. The calibrated input parameters (given in Table 2) were determined by considering the experimental data presented in Alvarado et al. [22]. The sphere properties are the interparticle friction coefficient (μ), the Young's modulus of the spherical particles (E_c), (this gives the contact normal stiffness as $K_N=4E_cR$, where R is the particle radius), the ratio of the shear to normal stiffnesses in the contact model (K_S/K_N). The parallel bond properties are the Young's modulus of the bonds, E_{pb}, the strengths of the parallel bonds in tension and in shearing (S^N_{pb} *and* S^S_{pb} respectively). The size of each parallel bond which is given by $\alpha_{bond}\, min(R_a,R_b)$, where R_a and R_b are the radii of the two contacting particles forming the bond, and the proportion of bonded contacts is λ. The PSDs of the two sandstones differed (Figure 6) and the calibration process resulted in slightly different contact parameters. In both cases in the DEM simulations, the particle diameters were scaled to reduce the numbers of particles in the simulations; the Castlegate DEM model had particle diameters that were 15 times those measured in the laboratory, while the Saltwash DEM model had particle diameters that were 9 times the laboratory values. Particles passing 63μm were assumed to form part of the cement and so were not modelled. The cylindrical samples considered were "carved" from dense rectangular samples that had been isotropically compressed to 10 MPa, and the bonds were installed once the cylindrical samples were brought to the required initial isotropic stress level for shearing. This carving procedure reduced the extent of the inhomogeneities that are inevitably induced along the boundaries, as discussed by Marketos and Bolton[23] as confirmed by careful calculation of the void ratio within selected internal sub-volumes. Figure 7 illustrates the stress-deformation response for the two materials at a confining pressure of 15 MPa, where σ'_1 and σ'_3 are the major and minor principal stresses respectively. In both cases, following an initial contraction, the samples exhibited dilation. The Castlegate specimen mobilized a peak stress ratio of 1.03 at an axial strain of 0.68%, while the Saltwash specimen mobilized a peak stress ratio of 0.8 at an axial strain of 0.56%. Both samples exhibit post-peak strain softening and as noted by Cheung [7],

local strain analysis and consideration of particle rotations indicate that localizations or shear bands do form in the samples.

Figures 8(a) and (b) consider the evolution of the CSDs with axial strain for both samples. As above, the CSD is the cumulative distribution by number of the constrictions. In each case the PSD (by volume) is indicated for comparison with the CSD and it is clear from Figure 8(a) that a small amount of the particles are sufficiently small to pass through the larger constrictions in the Saltwash model. For the Saltwash model, initially the C_{95} (95% of the constrictions are smaller than C_{95}), was 808μm, while at the final stage (5.5 % axial strain) the C_{95} had increased to 878 μm. Only about 1 % (by volume) of the particles are smaller than 800 μm. The minimum particle size in the Castlegate model was 1.05 mm and there were effectively no constrictions larger than this value. Thus it is unlikely that any suffusion (particle migration under fluid flow) could occur in these materials, as the geometrical criterion for suffusion, i.e. that the voids between particles are sufficiently large for the finer particles to migrate through them, is not met (assuming no particle crushing takes place).

While both samples exhibited an overall dilation during shearing, there was an initial contraction of both samples at the beginning of shearing (Figure 7(b)). The constriction sizes reflected this macro-scale response, referring to Figure 9(a), initially upon shearing there is a decrease in the representative constriction sizes, with this decrease being more marked in the Castlegate sample, subsequently there was a monotonic increase in constriction sizes, reflecting the (macro-scale) dilative volumetric strains evident in Figure 7(b). The initial volumetric contraction in the Castlegate sample was slightly greater than that in the Saltwash sample, however the data in Figure 9(b) indicate that the rate of decrease in median constriction size (C_{50}) with volumetric strain was significantly higher in the Castlegate sample than in the Saltwash sample. Referring to Figure 9(b), it is clear that once dilation starts the constriction size increases, but the relationship C_{50} and the volumetric strain differs in both samples; it is almost linear for the Saltwash sample, but it is non-linear for the Castlegate sample. It is also instructive to consider the number of constrictions. For a valid comparison the number of constrictions should be normalized by the system size. Figure 10(a) considers the constrictions normalized both by the number of particles in the samples and the number of contacts in the sample. Referring to Figure 10(a) whichever normalization is used, it is clear that the number of constrictions decreases non-linearly during shearing. When the number of constrictions is normalized by the number of contacts, the responses of the two specimens are almost indistinguishable, as illustrated in Figure 10(a); this is a likely consequence of the contact-based nature of the algorithm. Referring to Figure 10(b) is interesting to note that the relationship between the number of constrictions and the number of contacts is non-linear. Figure 10 (c) shows that both the number of contacts and the number of constrictions decrease as the sample dilates and the void space between the strong force chains opens out to form a smaller number of larger voids.

The orientations of the constriction normals give some insight into the anisotropy of the void space. Figures 11 and 12 present rose diagrams of the constriction normals for the Castlegate and Saltwash samples respectively at three key points: close to the point where the peak strength is mobilized, during the post-peak strain softening, and at the end of each simulation. At each strain level, three orthogonal views are presented (XY, XZ and YZ), and each bin in the rose diagram is coloured by the average diameter of the constrictions with normals orientated in that angular increment, normalized by the overall average constriction diameter. Thus the lengths of the bins give an indication of the anisotropy in terms of a directional bias in the number of constrictions, while the colours of the bins indicate directional bias in terms of constriction size. For both triaxial test simulations, pre-peak there is no obvious anisotropy associated with the constriction normal orientations. Referring to Figures 11 (a) to (c) and Figures 12(a) to (c), it is clear that there is a uniform distribution of orientations in all three views (XY, XZ and YZ) and the average constriction diameter in each bin lies close to the overall average value. Close to the peak (Figures 11(d) to (f) and Figures 12 (d) to (f)) there is a slight bias in the vertical views (XZ and YZ), and there appears to be slightly more constriction normals orientated with a preferential horizontal, rather than vertical orientation. At large strains (Figures 11 (g) to (i) and Figures 12 (g) to (i)) the observed anisotropies differ, depending on the sample. For the Castlegate sample, there is evidence of a bias in the constriction size, with the constrictions with vertically orientated normal vectors tending to be larger than the constrictions with horizontally orientated normals. No clear directional bias of constriction sizes is evident for the Saltwash sample. This may be a consequence of the smaller maximum axial strain value attained, or it may be related to the smaller anisotropy that was observed for the contact and parallel bond orientations as noted in Cheung [7] A detailed analysis considered the constriction sizes in increments and there is a preferential tendency for smaller constrictions to be horizontally orientated, while there is no orientation bias for the larger constrictions.

Conclusions

The work of Li and Li [3] who proposed a 2D algorithm for partitioning the void space was developed to enable partitioning of a 3D DEM dataset. The 3D implementation is more complex than the 2D case presented by Li and Li as the void phase is continuous and the individual voids are connected to each other. The partitions between individual void boundaries are objectively defined. The current implementation has focussed on defining the constrictions between voids and the 3D algorithm was compared with algorithms proposed by Reboul et al. [5] and Dong and Blunt [6], by applying it to DEM simulations that have been described by Barreto [4] and Barreto and O'Sullivan[18]. The comparison with these other methods indicated that the contact based method gives results that do not differ significantly from other available approaches. Of the alternative algorithms considered, the new contact based method was in closest agreement with the Reboul et al.

[5] algorithm using a overlap of 50%. The contact based method has the advantage of avoiding the rather subjective specification of an overlap that is associated with the Reboul et al. algorithm and it avoids the need to convert a DEM dataset to a 3D image format to apply the Dong and Blunt method as well as the associated sensitivity to the image resolution.

To illustrate the applicability of the 3D contact based algorithm, it was applied to the DEM simulations of cemented sand described by Cheung [7]. These simulations were originally carried out to calibrate DEM models of Castlegate and Saltwash sandstones with a view to studying sand production in reservoir sandstones. The data generated indicate that the size of the constrictions in both DEM models are smaller than the particles, thus, in the absence of particle crushing, any migration of sand particles though the pore network is unlikely. During shearing the constriction sizes mirrored the volumetric strain; they tended to decrease as the samples contracted and increase during dilation, however the magnitudes of the constriction size changes relative to the volumetric strain differed in both materials. The number of constrictions reduced as the sample dilated during shearing. While the distribution of the number of constrictions was relatively isotropic during shearing, the Castlegate sample exhibited a slight directional bias at large strain levels, with the larger constrictions having normals that are orientated in the direction of the major principal stress.

Acknowledgements

Dr. T. Shire's doctoral research was funded by an Engineering and Physical Sciences Research Council Doctoral Training Account Award. Dr. G. Cheung's doctoral research was co-sponsored by the Engineering and Physical Sciences Research Council and ARUP under the CASE for New Academics scheme.

References

[1] C. Thornton, Numerical simulations of deviatoric shear deformation of granular media, Géotechnique. 50 (2000) 43–53. doi:10.1680/geot.2000.50.1.43.

[2] M. Satake, Fundamental quantities in the graph approach to granular materials., in: J.T. Jenkins, M. Satake (Eds.), Mech. Granul. Mater. New Model. Const. Relations, Elsevier, New York, 1983: pp. 9–19.

[3] X. Li, X. Li, Micro-Macro Quantification of the Internal Structure of Granular Materials, J. Eng. Mech. 135 (2009) 641–656. doi:10.1061/(ASCE)0733-9399.

[4] D. Barreto Gonzalez, Numerical and expeirmental investigation into the behaviour of granular materials under generalised stress states, University of London, 2009.

[5] N. Reboul, E. Vincens, B. Cambou, A computational procedure to assess the distribution of constriction sizes for an assembly of spheres, Comput. Geotech. 37 (2010) 195–206. doi:10.1016/j.compgeo.2009.09.002.

[6] H. Dong, M. Blunt, Pore-network extraction from micro-computerized-tomography images, Phys. Rev. E. 80 (2009) 036307. doi:10.1103/PhysRevE.80.036307.

[7] L.Y.G. Cheung, Micromechanics of sand production in oil wells, University of London, 2010.

[8] M. Oda, S. Nemat-Nasser, J. Konishi, The Japanese Geotechnical Society NII-Electronic Library Service, Soils Found. 25 (1985) 85–97.

[9] R. Ghedia, C. O'Sullivan, Quantifying void fabric using a scan-line approach, Comput. Geotech. 41 (2012) 1–12. doi:10.1016/j.compgeo.2011.10.008.

[10] S. Beucher, C. Lantuejoul, Use of watersheds in contour detection, in: Proc. Int. Work. Image Process. CCETT, Rennes, Fr., 1979.

[11] T. Tsuchikura, M. Satake, "Statistical measure tensors and their application to computer simulation analysis of biaxial compression test., in: H., Murakami, J.E. Luco (Eds.), Eng. Mech. A Force 21st Century,, ASCE, New York, 1998: pp. 62–76.

[12] J. Konishi, F. Naruse, A note on fabric in terms of voids, in: M. Satake, J.T. Jenkins (Eds.), Micromechanics Granul. Mater. Proc., U.S.–Japan Semin. Micromechanics Granul. Mater., Elsevier, Amsterdam, Sendai-Zao, Ja, 1988: pp. 39–46.

[13] R. Al-Raoush, K. Thompson, C.S. Willson, Comparison of Network Generation Techniques for Unconsolidated Porous Media, 1700 (2003) 1687–1700.

[14] T. Shire, C. O'Sullivan, D. Barreto, G. Gaudray, Quantifying stress-induced anisotropy using inter-void constrictions, Geotechnique. (2013) 85–91. doi:10.1680/geot.11.T.020.

[15] T. Shire, Micro-scale Modelling of Granular Filters, Imperial College London, 2014.

[16] T. Shire, C.O. Sullivan, G. Gaudray, Comparison of two methods for measurement of soil constriction size distribution Key words, in: J.-J. Fry (Ed.), 6th Int. Conf. Scour Erosion, ICSE-6 Paris, August 27-31, 2012, SHF - Société Hydrotechnique de France, 2012.

[17] Mathworks, MATLAB, (n.d.).

[18] D. Barreto, C. O'Sullivan, The influence of inter-particle friction and the intermediate stress ratio on soil response under generalised stress conditions, Granul. Matter. 14 (2012) 505–521. doi:10.1007/s10035-012-0354-z.

[19] C. Thornton, Numerical simulations of deviatoric shear deformation of granular media, Géotechnique. 50 (2000) 43–53.

[20] L.Y.G. Cheung, C. O'Sullivan, M.R. Coop, Discrete element method simulations of analogue reservoir sandstones, Int. J. Rock Mech. Min. Sci. 63 (2013) 93–103. doi:10.1016/j.ijrmms.2013.07.002.

[21] D.O. Potyondy, P.A. Cundall, A bonded-particle model for rock, Int. J. Rock Mech. Min. Sci. 41 (2004) 1329–1364.

[22] G. Alvarado, N. Lui, M.R. Coop, Effect of fabric on the behaviour of reservoir sandstones, 1051 (2012) 1036–1051. doi:10.1139/T2012-060.

[23] G. Marketos, M. Bolton, Flat boundaries and their effect on sand testing, Int. J. Numer. Anal. Methods Geomech. 34 (2010) 821–837.

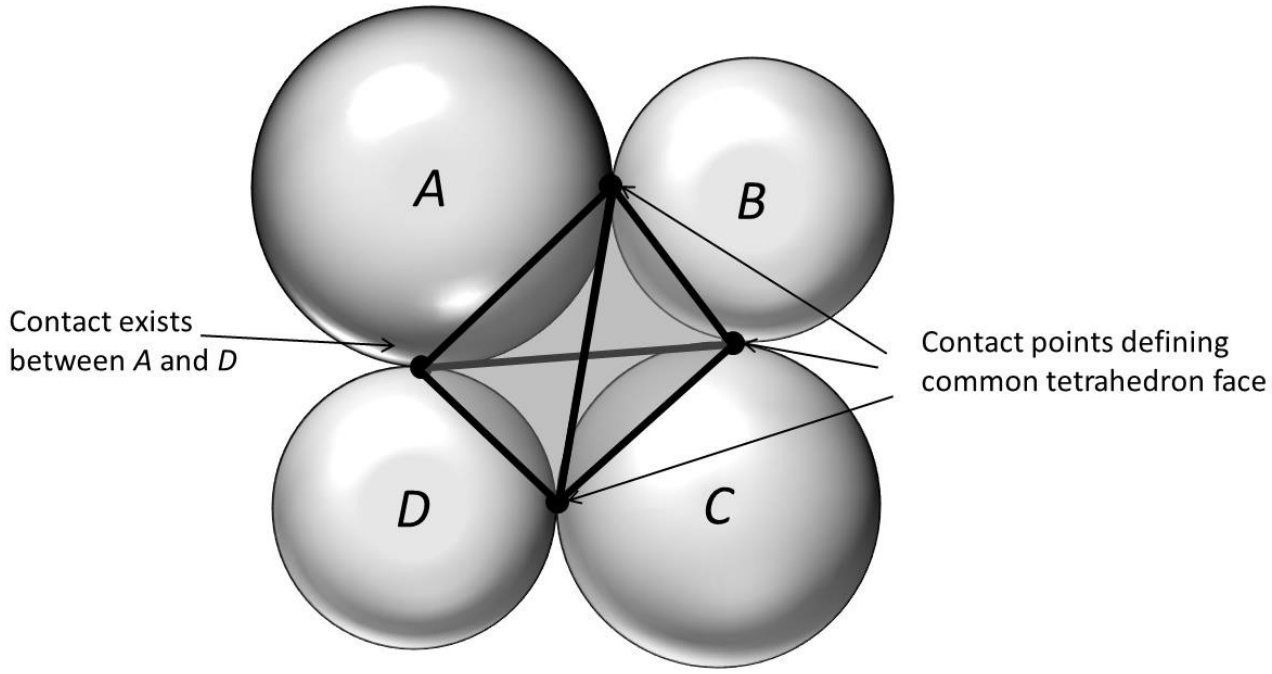

Figure 1– 4 particle constriction resulting in flat tetrahedron

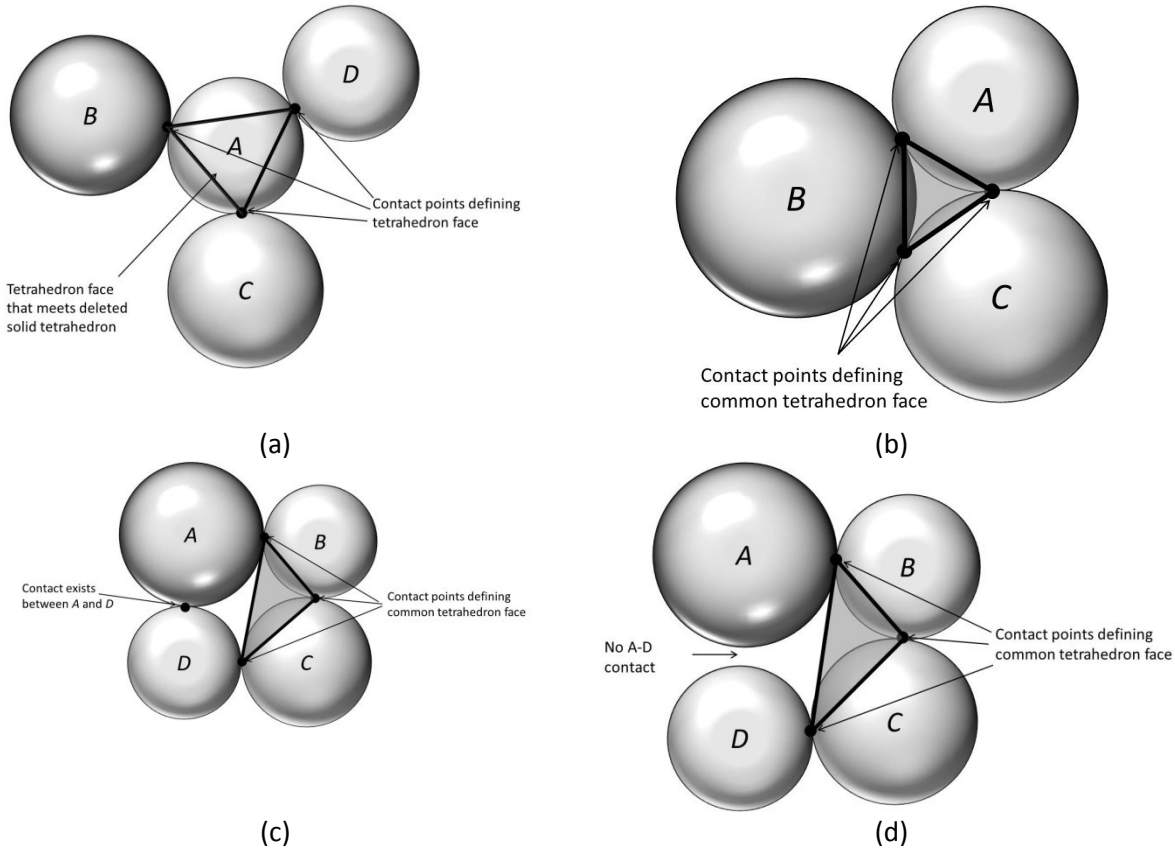

Figure 2: Cases defining void boundaries (a) Tetrahedron face in solid particle that clearly forms void boundary (b) 3-particle constriction (c) Closed loop of 4 particles defining a 4-particle constriction (d) Triangle face that does not fully describe constriction and that requires merging with adjacent triangle

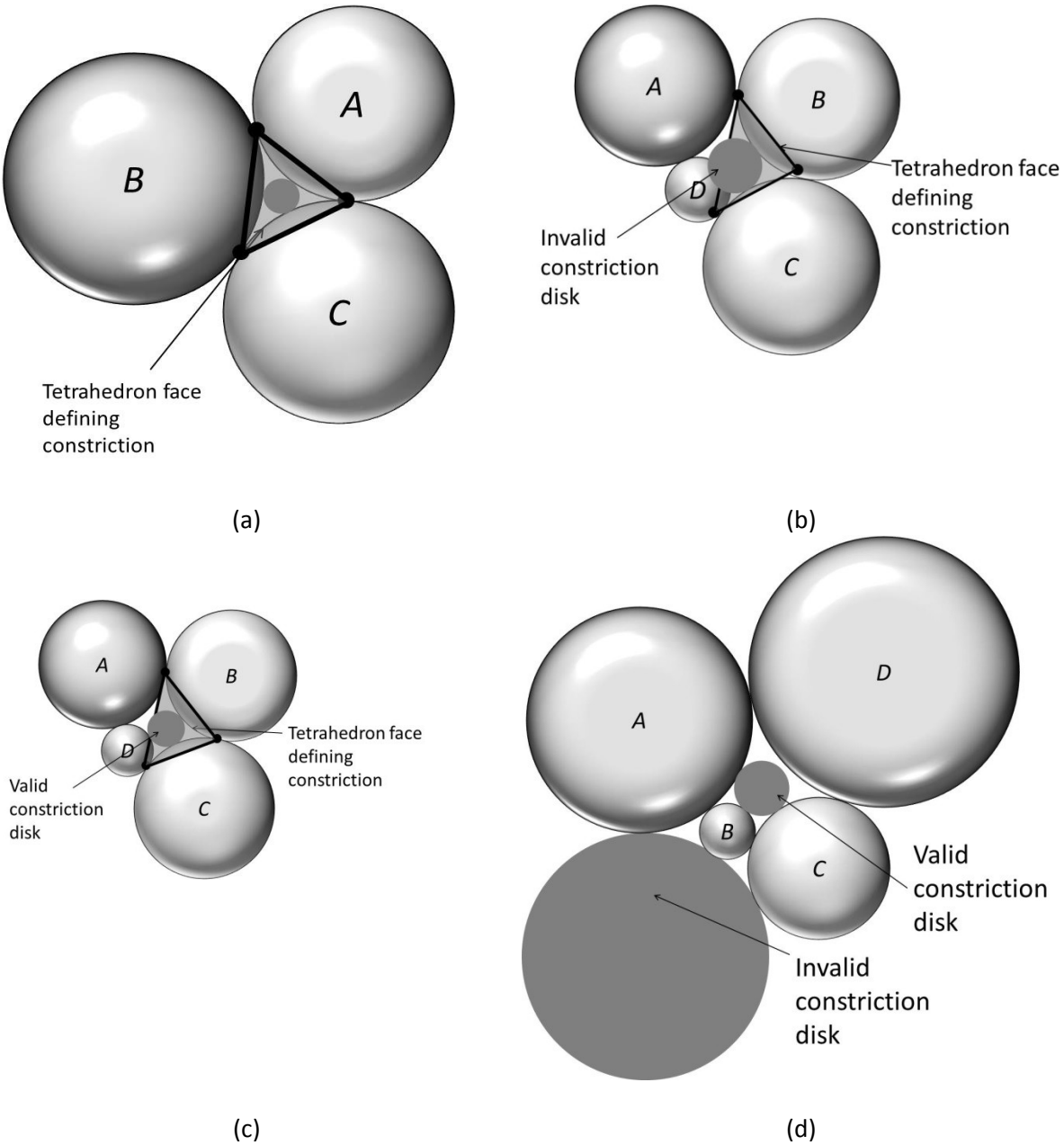

Figure 3: Illustration of constriction disks used to define constriction sizes: (a) Disk in 3-particle constriction (b) Invalid constriction disk in 4-particle constriction. (c) Valid constriction disk in 4-particle constriction (d) Illustration of erroneous constriction disk that may be generated in polydisperse materials

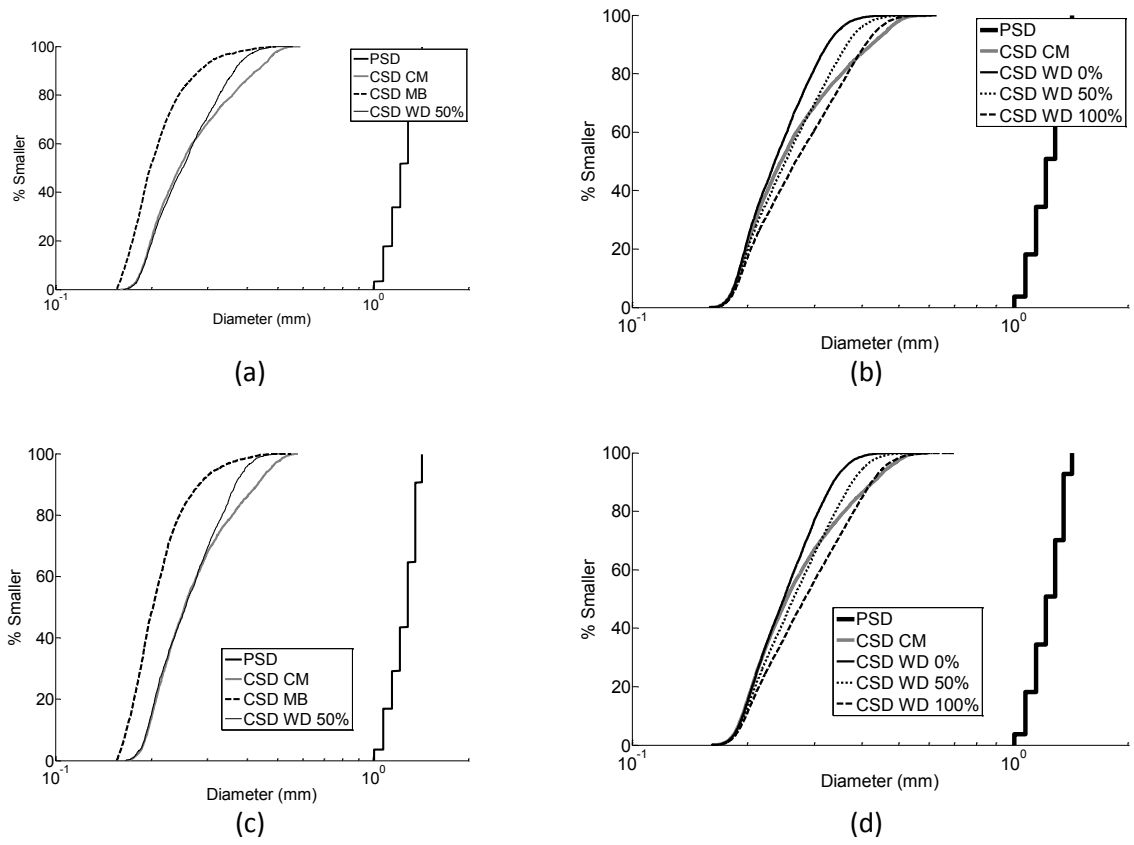

Figure 4: Comparison of constriction size distributions calculated for isotropic samples using various approaches: CM-Contact-based method propsed here, WD- Weighted Delaunay method Reboul et al. [5] , MB-Maximal Ball Dong and Blunt [6](a) Interior sub-volume for dense sample (μ=0) (b) full sample for dense packing (μ=0) (c) Interior sub-volume for loose sample (μ=0.325) (d) full sample for loose packing (μ=0.325)

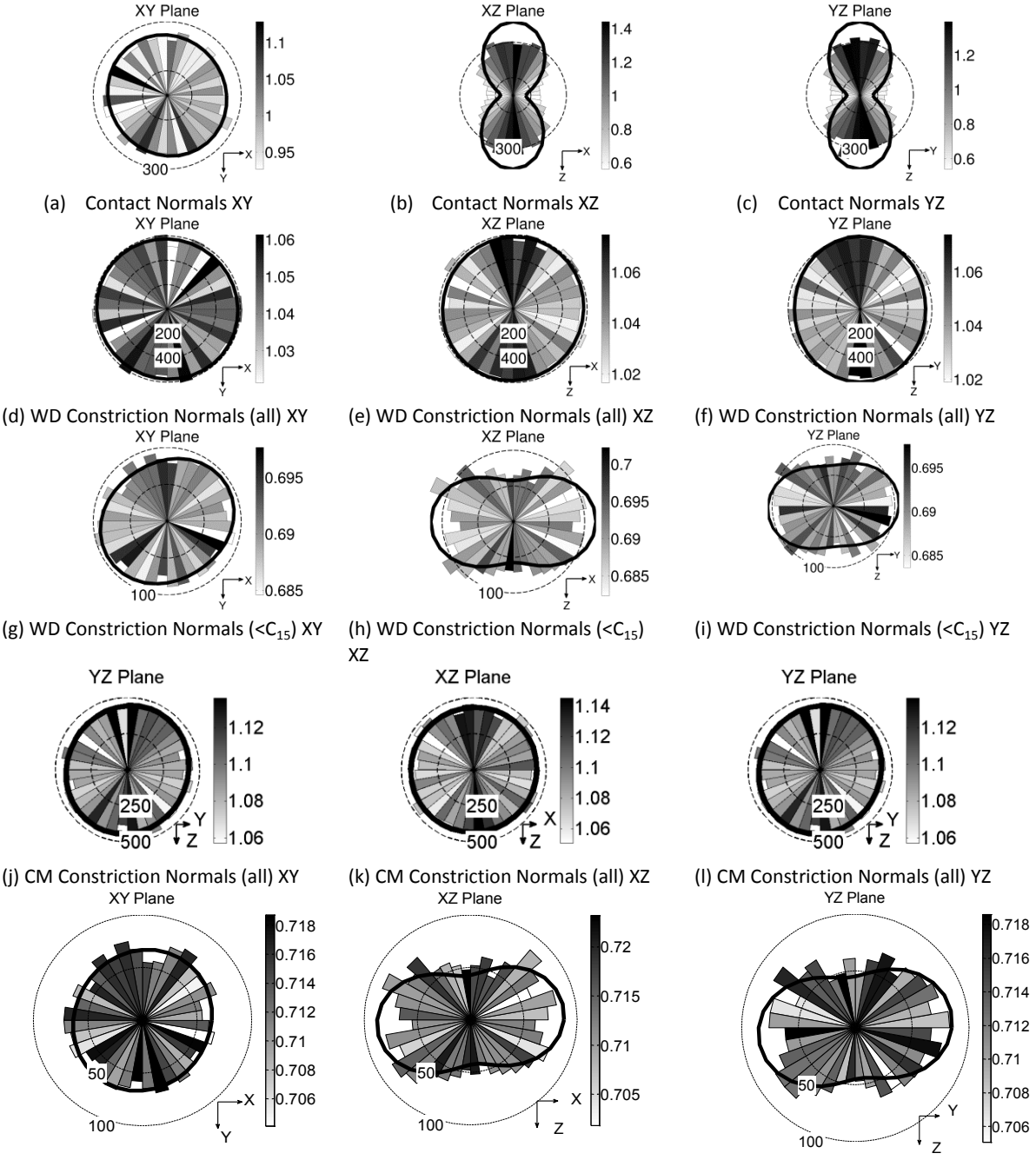

Figure 5: Rose diagrams of orientations for sample considered by Shire et al. (2013), triaxial compression ε_d=10%: (a-c) Contact normal orientations – bin shading indicates average contact force orientated within that bin normalized by overall average contact force. (d-i) Constriction normal orientations obtained using weighted Delaunay method (15% of constrictions are smaller than C_{15}) – bin shading illustrates constriction diameter orientated within that bin divided by overall average constriction diameter (j-o) Constriction normal orientations obtained using the contact-based method proposed here– bin shading illustrates constriction diameter orientated within that bin divided by overall average constriction diameter.

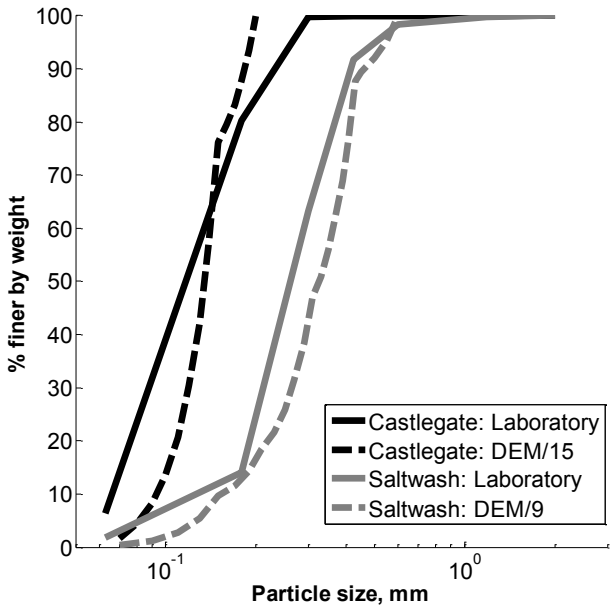

Figure 6: Particle size distributions for DEM simulations of triaxial compression tests on Saltwash and Castlegate samples (Cheung (2010), Alvadado et al. (2012))

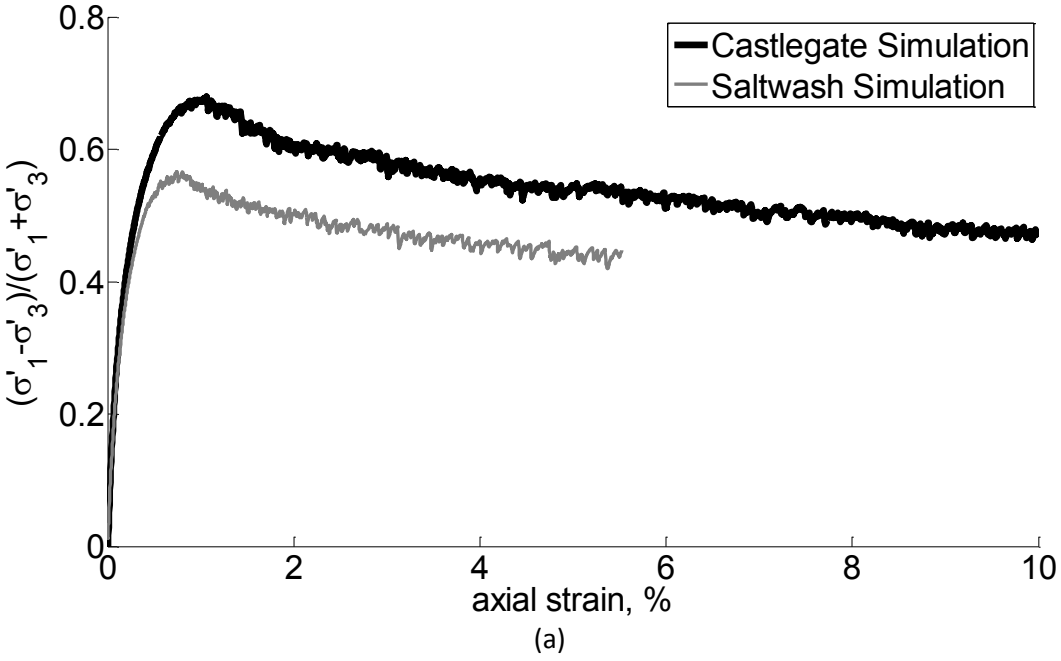

(a)

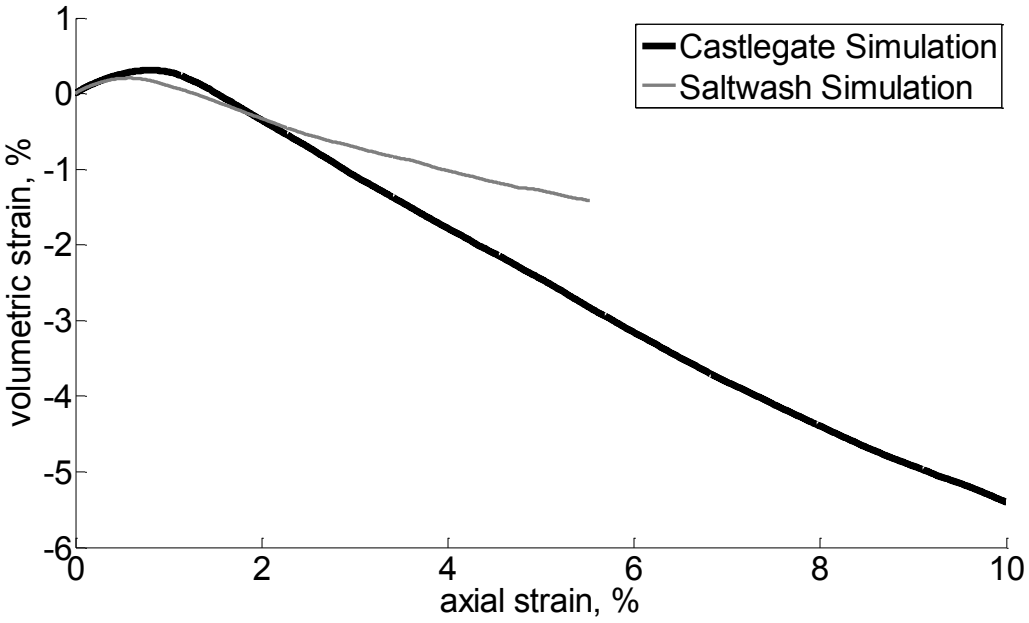

(b)

Figure 7: Stress:deformation response of simulated Castle gate and saltwash sandsones at 15 MPa confining pressure (a) Stress ratio versus axial strain (b) Volumetric strain versus axial strain

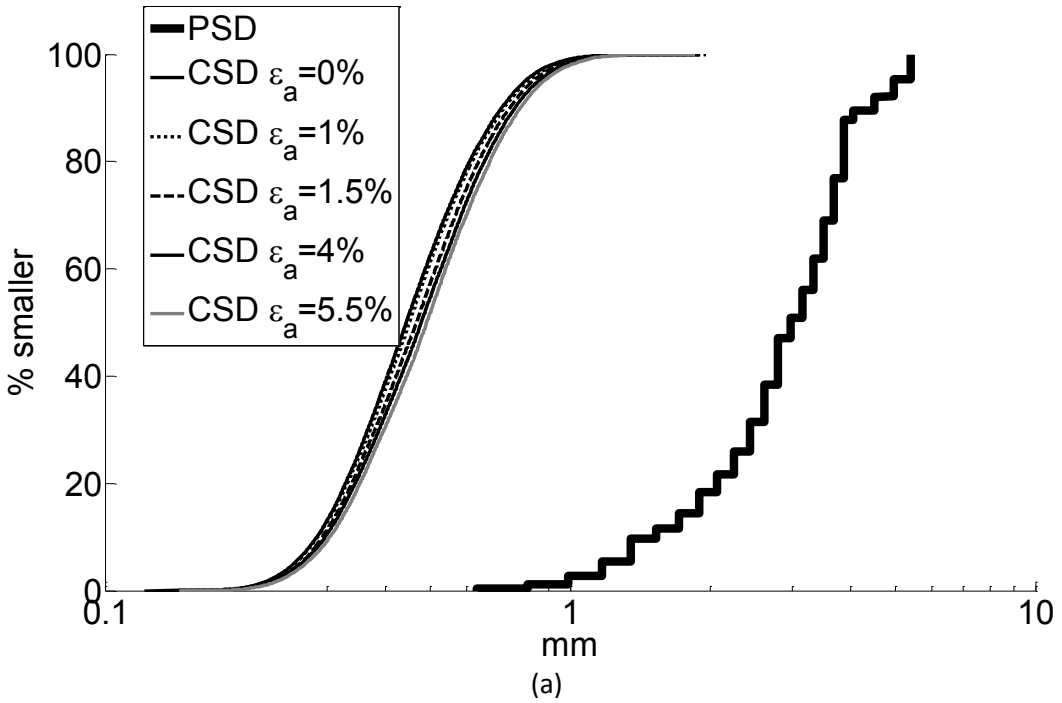

(a)

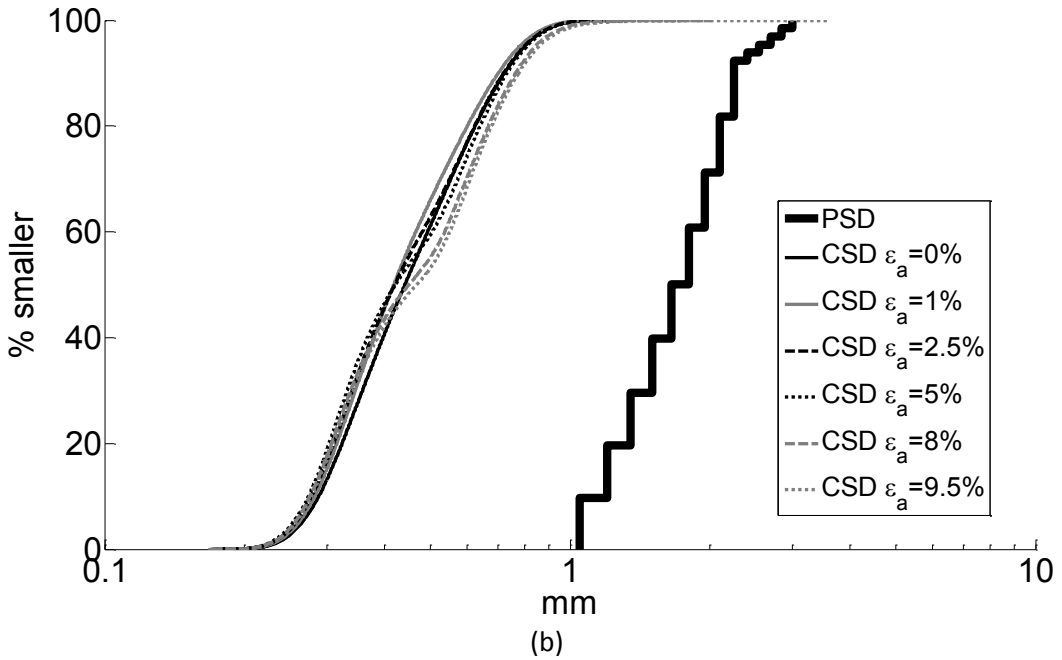

(b)

Figure 8 Variation of constriction size distribution during shearing (a) Saltwash sample (b) Castlegate sample

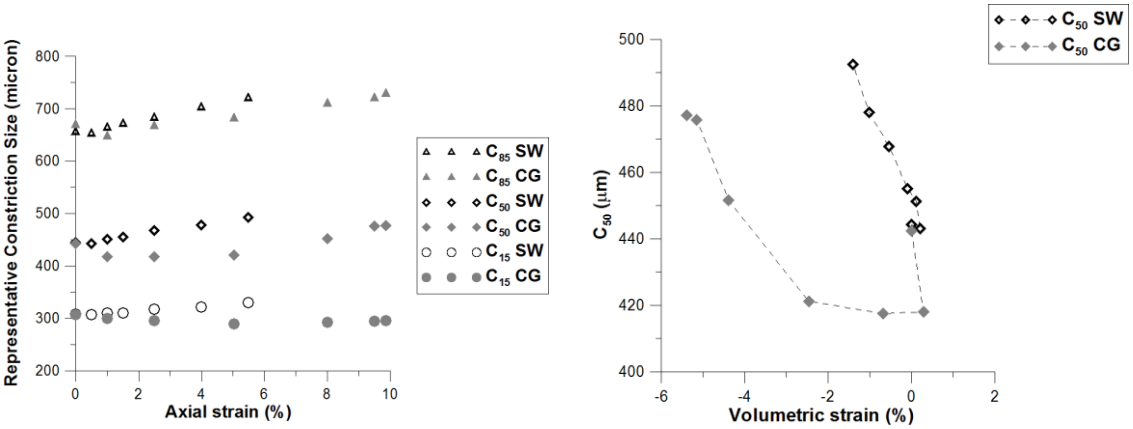

Figure9 Variation in constriction size during shearing for Saltwash (SW) and Castlegate (CG) samples (a) Reprentative constriction size versus axial strain (b) Median constriction size (C_{50}) versus volumetric strain.

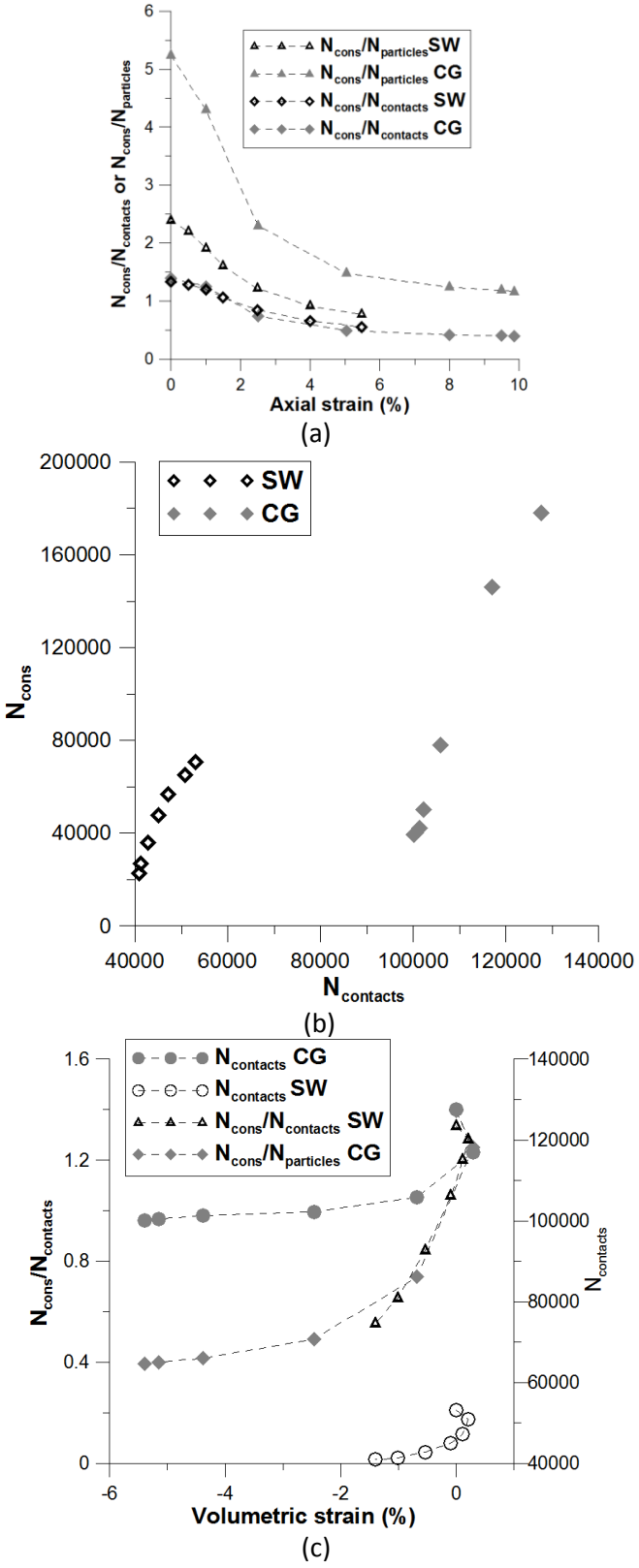

Figure 10: Variation in constriction size and number of constrictions during shearing for Saltwash (SW) and Castlegate (CG) samples

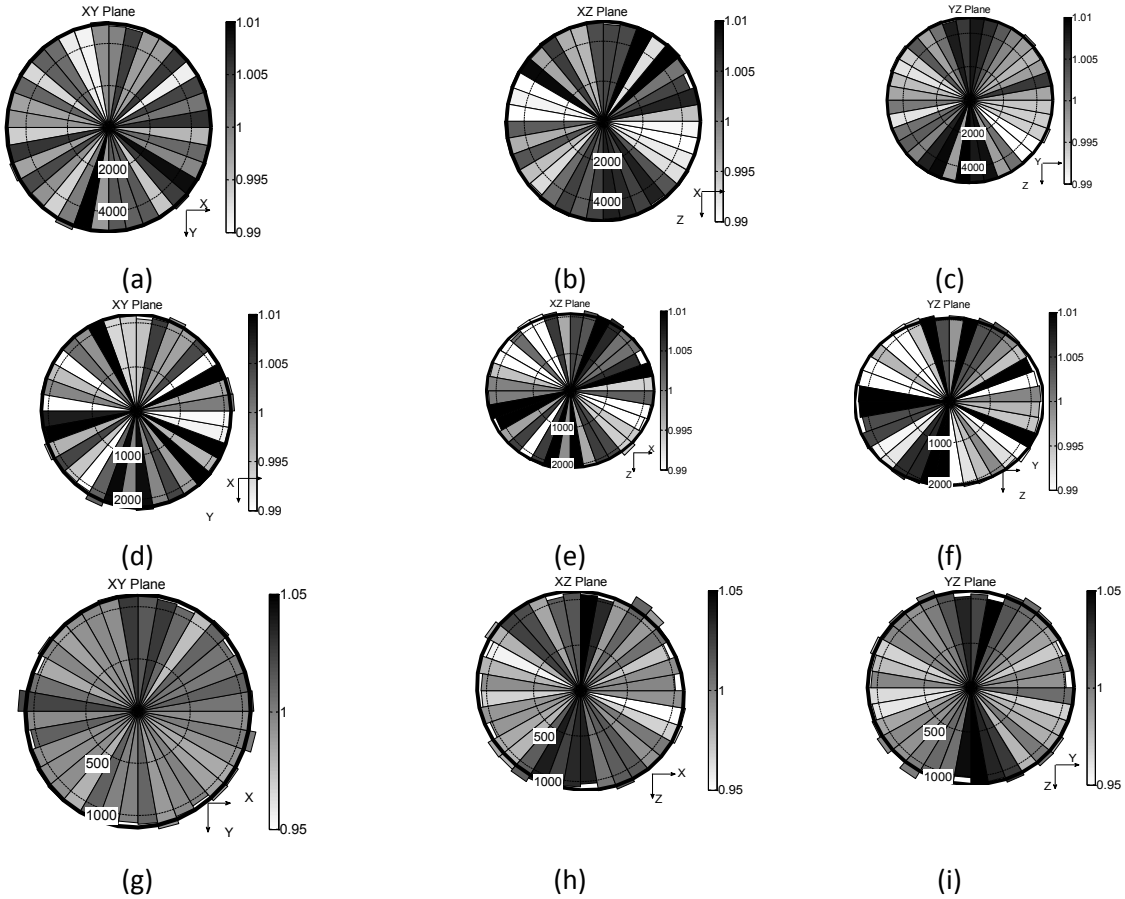

Figure 11: Rose Diagrams of constriction normal orientations, Castlegate sample: (a),(b),(c) axial strain 1%; (d),(e),(f) axial strain 2.5%; (g),(h),(i) axial strain 9.9%. Shading indicates average constriction size within angular increment, normalized by the overall average constriction size.

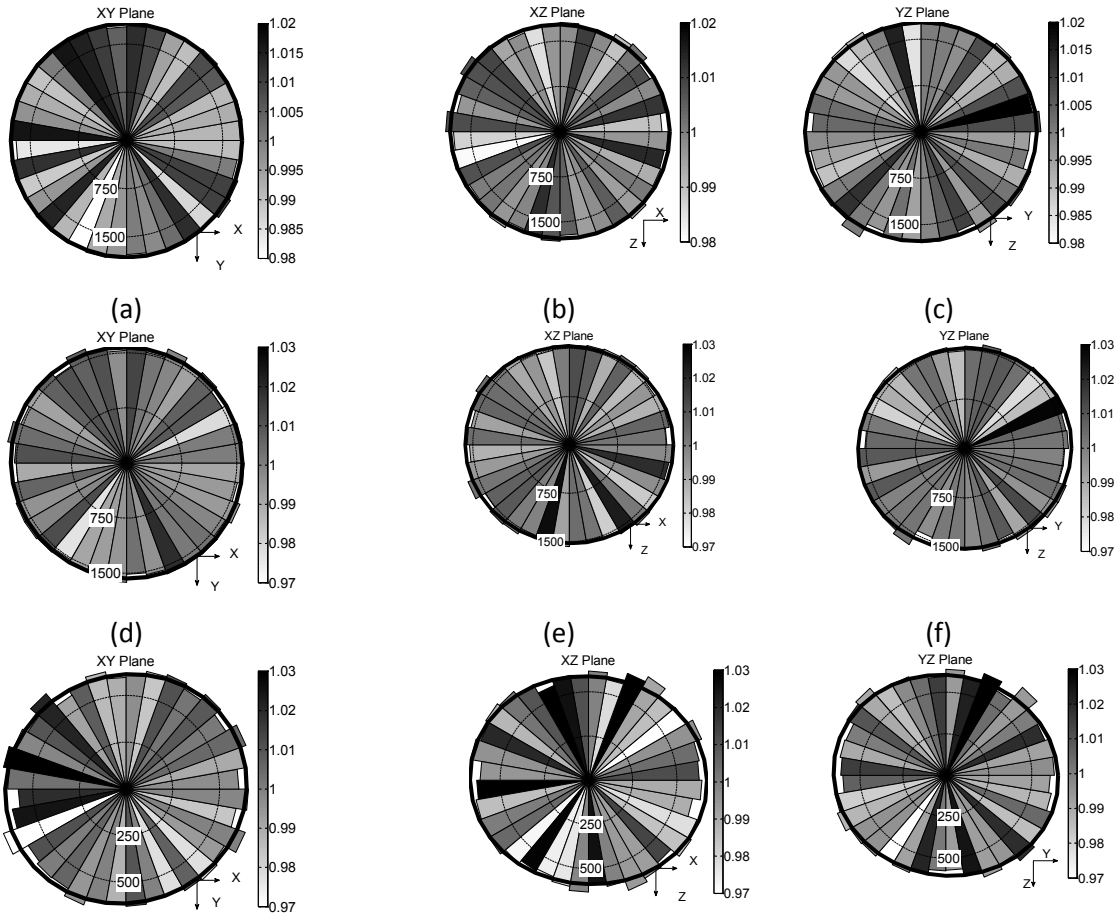

Figure 12: Rose Diagrams of constriction normal orientations, Saltwash sample: (a),(b),(c) axial strain 0.5%; (d),(e),(f) axial strain 1.0%; (g),(h),(i) axial strain 5.5%. Shading indicates average constriction size within angular increment, normalized by the overall average constriction size.

Table 1 Constriction data for glass ballotini samples – where N_{cons} is the number of constrictions, 50% of constrictions are smaller than C_{50}, 85% of constrictions are smaller than C_{85} and 15% of constrictions are smaller than C_{15}.

Sample	Contact-based method	Reboul et al. method 0% overlap	Reboul et al. method 50% overlap	Reboul et al. method 100% overlap	Dong and Blunt method
Dense, isotropic (μ=0.0) subvolume	N_{cons}=3,689 C_{50}= 0.245 mm C_{85}=0.390 mm C_{15}=0.194 mm		N_{cons}=2,030 C_{50}=0.250 mm C_{85}=0.344 mm C_{15}=0.195 mm		N_{cons}= 2,492 C_{50}=0.198 mm C_{85}=0.260 mm C_{15}=0.170 mm
Dense, isotropic (μ=0.0) full sample	N_{cons}= 14,218 C_{50}=0.245 mm C_{85}=0.385 mm C_{15}=0.194 mm	N_{cons}=11,250 C_{50}= 0.236 mm C_{85}=0.309 mm C_{15}=0.193 mm	N_{cons}=14,863 C_{50}=0.252 mm C_{85}=0.347 mm C_{15}=0.195 mm	N_{cons}=17,497 C_{50}=0.268 mm C_{85}=0.386 mm C_{15}=0.198 mm	
Loose, isotropic (μ=0.35) – sub-volume	N_{cons}= 3,098 C_{50}= 0.254 mm C_{85}=0.391 mm C_{15}=0.201 mm		N_{cons}= 1,892 C_{50}=0.256 mm C_{85}=0.351 mm C_{15}=0.200 mm		N_{cons}= 2,425 C_{50}=0.203 mm C_{85}=0.261 mm C_{15}= 0.172 mm
Loose, isotropic (μ=0.35) full sample	N_{cons}= 12,613 C_{50}=0.254 mm C_{85}=0.391 mm C_{15}=0.200 mm	N_{cons}=10,416 C_{50}= 0.249 mm C_{85}=0.321 mm C_{15}=0.200 mm	N_{cons}= 14,006 C_{50}=0.264 mm C_{85}=0.358 mm C_{15}=0.203 mm	N_{cons}=16,756 C_{50}=0.283 mm C_{85}=0.402 mm C_{15}=0.206 mm	

Table 2 Calibrated DEM Simulation Parameters for Castlegate and Saltwash Sandstones, Cheung et al. [20]

Sphere Properties – Castlegate		**Parallel-bond properties– Castlegate**	
E_c	20 GPa	E_{pb}	175 GPa
K_S/K_N	1	S^N_{pb}	1.25×10^6 kPa
μ	0.5	S^S_{pb}	1.5×10^6 kPa
Number of particles	34,007	α_{bond}	0.01-1.0
Radii of DEM particles	0.525 to 1.5 mm (follow PSD curve)	λ	0.5
Particle density	$265 \times 10^3 kg/m^3$		
Simulation System Parameters– Castlegate			
Timestep safety factor	0.2	Damping	0.0 during shearing
Sphere Properties– Saltwash		**Parallel-bond properties– Saltwash**	
E_c	20 GPa	E_{pb}	175 GPa
K_S/K_N	1	S^N_{pb}	1.00×10^6 kPa
μ	1.0	S^S_{pb}	1.20×10^6 kPa
Number of particles	29,369	α_{bond}	0.01-1.0
Radii of DEM particles	0.315 to 2.7 mm (follow PSD curve)	λ	0.4
Particle density	$265 \times 10^3 kg/m^3$		
Simulation System Parameters– Saltwash			
Timestep safety factor	0.2	Damping	0.0 during shearing